Unconventional Spin Pumping and Magnetic Damping in an Insulating Compensated Ferrimagnet

Yan Li, Dongxing Zheng, Bin Fang, Chen Liu, Chenhui Zhang, Aitian Chen, Yinchang Ma, Ka Shen, Haoliang Liu, Aurelien Manchon, et al.

Unconventional spin pumping and magnetic damping in an insulating compensated ferrimagnet

Yan Li, Dongxing Zheng, Bin Fang, Chen Liu, Chenhui Zhang, Aitian Chen, Yinchang Ma, Ka Shen, Haoliang Liu, Aurélien Manchon, and Xixiang Zhang**

Y. Li, D.-X. Zheng, B. Fang, C. Liu, C.-H. Zhang, A.-T. Chen, Y.-C. Ma, Prof. A. Manchon, X.-X. Zhang
Physical Science and Engineering Division, King Abdullah University of Science and Technology, Thuwal 23955–6900, Saudi Arabia
Email: xixiang.zhang@kaust.edu.sa

Prof. K. Shen
The Center for Advanced Quantum Studies and Department of Physics, Beijing Normal University, Beijing 100875, China
Email: kashen@bnu.edu.cn

Prof. H.-L. Liu
School of Science, Harbin Institute of Technology, Shenzhen 518055, China

Prof. A. Manchon
Aix-Marseille Université, CNRS, CINaM, Marseille, France

Keywords: spin pumping, magnetic damping, coherent and incoherent spin currents, handedness, insulating compensated ferrimagnet

Abstract

Recently, the interest in spin pumping has escalated from ferromagnets into antiferromagnetic systems, potentially enabling fundamental physics and magnonic applications. Compensated ferrimagnets are considered alternative platforms for bridging ferro- and antiferromagnets, but their spin pumping and the associated magnetic damping have been largely overlooked so far despite their seminal importance for magnonics. Herein, we report an unconventional spin pumping together with magnetic damping in an insulating compensated ferrimagnet $Gd_3Fe_5O_{12}$. Remarkably, we unambiguously identified the divergence of the nonlocal effective magnetic damping induced by spin pumping close to the compensation temperature in $Gd_3Fe_5O_{12}$/Cu/Pt heterostructures. Furthermore, the coherent and incoherent spin currents, generated by spin pumping and spin Seebeck effect respectively, undergo a distinct direction change with the variation of temperature. The physical mechanisms underlying these observations are self-consistently clarified by the ferrimagnetic counterpart of spin pumping and the handedness-related spin-wave spectra. Our findings broaden the conventional paradigm of the ferromagnetic spin pumping model and open new opportunities for exploring the ferrimagnetic magnonic devices.

Introduction

Magnonics, a research field centered on spin waves/currents, has enabled the conception and the exploitation of low-dissipation and high-performance magnetic storage and computational devices[1-3]. Spin pumping (SP) induced by ferromagnetic resonance (FMR) provides an efficient route for generating and driving spin currents into a nonmagnetic material from a ferromagnetic spin reservoir while exerting a magnetic damping-related torque on magnetization[4-7]. Recently, the interest in SP in antiferromagnets has surged with the rapid progress of the antiferromagnetic spintronics/magnonics[8-10]. In contrast to ferromagnets only hosting the right-handed mode, the coexisting left- and right-handed precession modes in antiferromagnets add a new paradigm in manipulating chiral magnons and further encoding information through polarization, amplitude, and phase[11, 12]. On the other side of the coin, the vanishing net magnetization in antiferromagnets, as well as the resonance frequency up to the terahertz regime, raise hurdles in the excitation of magnetization dynamics and the detection of SP[13, 14]. Alternatively, compensated ferrimagnets, which host two inequivalent magnetic sublattices with antiferromagnetic interaction, exhibit quasi-antiferromagnetic behavior close to the compensation points and quasi-ferromagnetic characteristics far away from the compensation points[15-17]. Thus, compensated ferrimagnets stand out as a fertile platform to combine the benefits of both ferro- and antiferromagnets in potential device applications[18-20]. However, thus far, SP from compensated ferrimagnets and the associated magnetic damping have been largely overlooked in spite of their seminal importance for magnonic device development.

Yttrium iron garnet, $Y_3Fe_5O_{12}$ (YIG), is commonly regarded as a ferromagnet because of the strong antiferromagnetic coupling between the *a*-Fe and *d*-Fe sublattices[21]. By replacing the nonmagnetic element Y with the magnetic rare-earth element Gd, an insulating compensated ferrimagnet, $Gd_3Fe_5O_{12}$ (GdIG), is constructed with finite net magnetization. The antiparallel aligning moments of Gd and Fe cancel each other at the magnetic compensation temperature (T_M), resulting in the vanishing of the net magnetization[22]. Like antiferromagnets, spin dynamics in GdIG provide the left- and right-handed precession modes, which evolve with the temperature variation[23-25]. In addition, spin angular momentum can be transferred by the magnon spin current without involving charge current between the GdIG films and the adjacent

materials, although GdIG is electrically insulating[26]. Such an insulating compensated ferrimagnet provides a promising platform for exploring ferrimagnetic spin dynamics and low-dissipation magnonic devices. Here, we report an unconventional SP and the associated magnetic damping in GdIG-based heterostructures. We established that the bulk magnetic damping, as well as the SP-related nonlocal magnetic damping, both dramatically increased when the temperature approached T_M. Furthermore, the different variations in the properties of coherent and incoherent spin currents with temperature were examined by comparing the results of the SP and spin Seebeck effect (SSE) experiments. The underlying mechanisms are well understood by the ferrimagnetic SP model and the modification of the handedness-related spin-wave spectra when changing the temperature.

Results and discussions

35 nm-thick $Gd_3Fe_5O_{12}$ (GdIG) films were epitaxially grown on (111)-oriented substituted gadolinium gallium garnet substrates (sGGG) by pulsed laser deposition (PLD). The crystal quality was characterized using scanning transmission electron microscopy (STEM). In Figure 1a, the sharp interface between the GdIG film and the sGGG substrate can be clearly observed from the STEM cross-sectional image in the high-angle annular dark-field mode. There was no elemental intermixing at the interface, as determined by the energy-dispersive X-ray spectroscopy (EDX) mapping of the Fe atoms in the same area, as shown in Figure 1b. The atomic-resolution STEM image in Figure 1c exhibits a good epitaxial relationship between the substrate and the GdIG film with an atomically sharp interface. A set of diffraction patterns corresponding to Figure 1c is shown in Figure 1d.

Figure 1f presents hysteresis loops with the in-plane magnetic field measured at different temperatures after subtracting the paramagnetic background of the substrate. The saturation magnetization, M_s, extracted from the loops, is plotted in Figure 1g as a function of temperature. The net magnetization of GdIG almost vanishes at the T_M of ~200 K. In reality, GdIG consists of three magnetic sublattices: an octahedral Fe sublattice (*a* sites), a tetrahedral Fe sublattice (*d* sites) and a dodecahedral Gd sublattice (*c* sites), as shown in Figure 1e. The two Fe sublattices can be treated as one effective Fe magnetic sublattice because of their robust antiferromagnetic superexchange. As illustrated in the insets of Figure 1g, the Gd sublattice is antiferromagnetically coupled to the effective Fe sublattice, and the effective Fe (Gd) sublattice

dominates the net magnetization above (below) T_M. The high-quality single-crystalline GdIG film with a magnetic compensation temperature offers an excellent platform for studying the magnetic damping and spin transport across the interface in ferrimagnets.

To investigate the spin dynamics in GdIG films, we conducted in-plane FMR measurements[27]. Here the low-frequency uniform mode, regarded as the ferromagnetic counterpart[28], was triggered by the absorption of radiofrequency/microwave radiation, as illustrated in Figure 2a. Figure 2b shows the typical FMR spectra recorded as a function of the in-plane magnetic field (H) at various frequencies at 300 K, from which the resonant magnetic field (H_r) and linewidth (ΔH) can be obtained. The magnetic damping manifests itself in the resonant linewidth in the FMR experiments. Figure 2c shows plots of the extracted resonant frequency (f) versus H_r for the GdIG film. The dispersion relations between f and H_r at various temperatures display different characteristics, which can be described by the Kittel formula[29]:

$$f = \frac{g\mu_0\mu_B}{h}\sqrt{H_r(H_r + M_{eff})}. \quad (1)$$

Here, h, μ_0, μ_B, g, and M_{eff} are the Plank constant, vacuum permeability, Bohr magneton, Landé g-factor and effective magnetization, respectively. As plotted in Figure 2d, the extracted value of ΔH from the FMR spectra depends linearly on the frequency with different slopes analyzed for the different temperatures. This suggests that the magnetic relaxation of GdIG films is properly represented by Gilbert damping. The Gilbert damping can be decomposed into two contributions: a bulk contribution involving magnon – magnon and magnon – phonon scattering, and an interfacial contribution arising from the SP and the magnetic proximity effect (MPE) at the interface[6, 30-32]. Furthermore, the interfacial damping from the SP is generally termed as nonlocal magnetic damping[4, 33]. Accordingly, the values of the Gilbert damping (α) can be extracted by fitting the data of ΔH and f using the following equation[34],

$$\Delta H = \Delta H_0 + \frac{2h\alpha}{g\mu_0\mu_B} f, \quad (2)$$

where ΔH_0 is the inhomogeneous linewidth broadening. Eq. 2 was employed to obtain the Gilbert damping for all the samples.

To explore the interfacial magnetic damping, a Pt layer with a thickness of 10 nm, which is larger than the spin diffusion length of Pt ~1-8 nm[35], was deposited on the GdIG (thickness: 35 nm) film. Thereafter, the GdIG/Pt sample was subjected to FMR measurements. As shown in Figure 2e, the linewidth of the FMR spectra at 6 GHz for GdIG/Pt is noticeably enhanced

compared to that for GdIG. The inset in Figure 2e displays f versus H_r at 375 K. The extracted ΔH as a function of H_r is shown in Figure 2f for the GdIG and GdIG/Pt films. Evidently, the slope of the linear ΔH versus f plot for the GdIG/Pt sample is larger than that for the GdIG sample. The data shown in Figures 2e and 2f indicate that the Pt layer introduces additional damping.

The temperature dependence of the Gilbert damping ($\alpha_{GdIG}(T)$) for the GdIG film is presented in Figure 3a. The damping values were calculated to be 3.3×10^{-3} and 5.8×10^{-3} at the lowest temperature (10 K) and the highest temperature (375 K) in our experiments, respectively. The rather low damping values on the order of 10^{-3}, observed at low (10 K) and high (375 K) temperatures can be attributed to the fact that the magnon–magnon and magnon–phonon scattering processes dominate the magnetic relaxation process, whereas the magnon–electron scattering is suppressed because of the absence of conduction electrons in the insulating GdIG film[31]. Although these two values are quite similar and small, considerably larger damping values (one order of magnitude higher than those observed at 10 K and 375 K) were obtained when the temperature approached T_M from both directions. Evidently, the Gilbert damping significantly increases when the temperature approaches T_M. This divergent temperature dependence of the damping close to T_M is in stark contrast with that in ferromagnets, whose damping commonly decreases upon cooling[36]. As derived in Supporting Information (SI), the effective Gilbert damping (α_{eff}) in ferrimagnets can be expressed as $\alpha_{eff} = \frac{\alpha_1 L_1 + \alpha_2 L_2 + \delta}{|L_1 - L_2|}$. Here, δ, L_i, and α_i represent the off-diagonal term of the damping, angular momentum and Gilbert damping of the magnetic sublattice (i [i = 1, 2 = Fe, Gd]), respectively. The equation indicates that the effective Gilbert damping diverges at the compensation temperature (T_A) of a ferrimagnet, where two angular momenta are equal ($L_{Fe} = L_{Gd}$). Consequently, because T_A is close to T_M in GdIG[37], a divergent damping was reported close to T_M in our FMR measurements.

The temperature dependence of the damping in GdIG/Pt is very similar to that of GdIG, as shown in Figure 3a. Noticeably, compared to the damping of the GdIG film (α_{GdIG}), an enhancement of the effective Gilbert damping, $\Delta\alpha(\alpha_{GdIG/Pt} - \alpha_{GdIG}) > 0$, is clearly observed for the GdIG/Pt film over the entire temperature range, suggesting that the GdIG/Pt interface substantially contributes to the overall damping. In analogy with the damping enhancement in

ferromagnet/normal metal multilayers, the damping enhancement in ferrimagnet/Pt films may be derived from SP and MPE[30]. Pt can have a spontaneous magnetic moment at the interface with a ferromagnet owing to its large Stoner enhancement[38, 39]. The polarized Pt layer possesses a large damping owing to the strong spin-orbit interaction of Pt. Thus, the effective damping in the effective ferromagnet, composed of the polarized Pt layer and GdIG film, is larger than that in a single GdIG film. This is the so-called enhancement of the damping from MPE. Another route for the damping enhancement is the nonlocal damping induced by SP. The magnetization precession of GdIG triggered by microwave results in a nonequilibrium chemical potential imbalance of the spins at the GdIG/Pt interface, causing an angular momentum flow (spin currents) from GdIG to Pt. The nonlocal absorption of the pumped spin current by the Pt layer, owing to the Elliott – Yafet and Dyakonov – Perel spin relaxation, results in the enhancement of the Gilbert damping[6, 40].

To exclude the contribution from MPE, a 5 nm-thick Cu spacer with a negligible spin-orbit interaction and a long spin diffusion length was inserted to obstruct the MPE between the GdIG and the Pt layers[30, 41, 42]. The temperature-dependent damping in the GdIG/Cu/Pt sample is also plotted in Figure 3a. A diverging damping versus temperature curve is observed for GdIG/Cu/Pt. Note that the transmission of spin currents across the interfaces can be affected in some extent when the polarized Pt layer is replaced with the Cu layer[43-45]. The effective Gilbert damping contributed by the MPE is approximatively estimated by $\Delta\alpha_{MPE} = \alpha_{GdIG/Pt} - \alpha_{GdIG/Cu/Pt}$ [see SI][30, 42, 46]. As shown in Figure 3b, $\Delta\alpha_{MPE}(T)$ is nearly independent of temperature with very small values. The nonlocal damping contributed by SP is evaluated by $\Delta\alpha_{SP} = \alpha_{GdIG/Cu/Pt} - \alpha_{GdIG}$. Different from the behavior of $\Delta\alpha_{MPE}(T)$, $\Delta\alpha_{SP}(T)$ increases as the temperature approaches T_M from both sides, as shown in Figure 3b. Moreover, $\Delta\alpha_{MPE} = 1.2 \times 10^{-3}$ is twice smaller than $\Delta\alpha_{SP} = 2.7 \times 10^{-3}$, as exemplified by the magnetic damping at 300 K. Furthermore, the values of $\Delta\alpha_{MPE}(T)$ are almost negligible below T_M. Therefore, SP plays a dominant role in the enhancement of the effective Gilbert damping in GdIG/Pt, particularly below T_M. In ferrimagnet with two magnetic sublattices, the spin current, $\boldsymbol{I}_s$, generated by SP is given by $\boldsymbol{I}_s = \frac{\hbar}{e}\sum_{i,j=1,\ 2} G_{ij}\boldsymbol{m}_i \times \dot{\boldsymbol{m}}_j$, where G_{ij} and $\boldsymbol{m}_i$ denote the spin-mixing conductance matrix and the unit vector of the magnetic moment of sublattice i,

respectively[15, 47]. That is, the spin currents can be treated as the sum of two independent SP processes in the two magnetic sublattices and the inter-sublattice contributions, implying that the Gilbert-type terms (damping-like torque) should be added to the Landau – Lifshitz – Gilbert equation. Note that the magnetic moment of Gd originates from the inner 4*f* shells, which are more localized compared to the 3*d* shells of Fe. Consequently, the angular momentum transfer between Pt and GdIG is dominated by the effective Fe sublattice *via s-d* exchange. Therefore, the SP-driven damping ($\Delta\alpha_{SP}$) can be simplified as $\Delta\alpha_{SP} \approx \frac{\Delta\alpha_{Fe}L_{Fe}}{|L_{Fe}-L_{Gd}|}$. Here, $\Delta\alpha_{Fe}$ denotes the damping enhancement induced by SP in the effective Fe sublattice. This suggests that $\Delta\alpha_{SP}$ diverges at temperature close to T_A, which is consistent with our experimental results shown in Figure 3b.

To further elucidate the difference in SP between ferrimagnets and ferromagnets, we characterized the efficiency of the interfacial spin transport parameterized by the spin-mixing conductance. Assuming that the SP-related damping obeys the classical spin pumping in ferromagnetic systems, the effective spin-mixing conductance is determined by[6] $\Delta\alpha_{SP} = \frac{g\mu_B}{4\pi M_s t_{GdIG}} G_{FM}^{\uparrow\downarrow}$. Here, t_{GdIG} and M_s are the thickness and saturation magnetization of the GdIG film, respectively. The cyan curve in Figure 3b displays temperature-dependent $G_{FM}^{\uparrow\downarrow}$. The obtained $G_{FM}^{\uparrow\downarrow}$ is 0.9×10^{18} m^{-2} at 375 K. As the temperature decreases, $G_{FM}^{\uparrow\downarrow}$ almost monotonically increases and reaches up to 3.4×10^{19} m^{-2} at 25 K. Note that at 25 K, $G_{FM}^{\uparrow\downarrow}$ sharply increases by ~40 times relative to the value at 375 K. Such a dramatic increase in $G_{FM}^{\uparrow\downarrow}$ is elusive and even unreasonable, particularly considering the weak SP efficiency between the Gd sublattice and the Pt layer, as well as the Gd sublattice dominating the net magnetization of GdIG at low temperatures. Essentially, the angular momentum transfer predominantly occurs between the effective Fe sublattice and Pt. Therefore, the enhanced damping ($\Delta\alpha_{Fe}$) and the magnetization (M_{Fe}) of the Fe sublattices should replace $\Delta\alpha_{SP}$ and M_s in Eq. 6, respectively. According to the SP model in ferrimagnets [see SI], the spin mixing conductance ($G_{FiM}^{\uparrow\downarrow}$) is estimated by $\Delta\alpha_{Fe} = \frac{g\mu_B}{4\pi M_{Fe} t_{GdIG}} G_{FiM}^{\uparrow\downarrow}$. As shown in Figure 3b, the values of $G_{FiM}^{\uparrow\downarrow}$ are $(2-9) \times 10^{18}$ m^{-2} over the temperature range, which are comparable with the values for YIG/Pt[48-50]. Consequently, the significant difference between $G_{FM}^{\uparrow\downarrow}$ and $G_{FiM}^{\uparrow\downarrow}$ further verifies

that the ferrimagnetic counterpart of SP should be carefully considered in ferrimagnetic systems, particularly in compensated rare earth-transition element ferrimagnets.

To gain further insights on the SP from compensated ferrimagnets, we measured the spin current under the FMR condition for the GdIG/Pt film. The uniform magnetization precession of GdIG excites coherent spin waves that inject spin angular momentum (spin currents, $\boldsymbol{j_s}$) into the adjacent Pt layer, in which a charge current ($\boldsymbol{j_c}$) can be generated *via* the inverse spin Hall effect (ISHE) due to the strong spin-orbit coupling in Pt[51], as schematically drawn in Figure 4a. Figure 4b displays the SP-driven ISHE voltage signals ($V_{SP}(H)$) nearby FMR condition at sweeping positive (black) and negative (red) magnetic fields at a excitation frequency of 6 GHz at 375 K. The V_{SP} versus H curves exhibit a resonant Lorentzian line shape, and its sign reverses as the polarity of the sweeping magnetic field changes, confirming the ISHE origin following the relationship $\boldsymbol{j_c} \propto \boldsymbol{j_s} \times \boldsymbol{\sigma}$ with the spin polarization $\boldsymbol{\sigma}$. Figure 4c shows the microwave power dependence of $V_{SP}(H)$ at f = 6 GHz. As shown in the inset of Figure 4c, the extracted amplitudes of the $V_{SP}(H)$ scale linearly with the microwave power (P), indicating that the observed SP-induced ISHE is in the linear regime. The ISHE spectra were also measured at varying temperatures, and all exhibit a resonant Lorentzian line shape with a negative amplitude in the sweeping positive magnetic field, as shown in Figure 4d.

Spin current injection by incoherent spin waves can be triggered by applying a thermal gradient across the interface, *via* an effect called longitudinal SSE[52, 53]. As schematically shown in Figure 4e, an insulating SiO_2 layer was heated by a Ti/Pt strip with a charge current, giving rise to a temperature gradient (∇T) along the z axis. The incoherent spin waves induced by the ∇T *via* the SSE carry spin angular momentum into the adjacent Pt layer. The voltage signals [$V_{SSE}(H)$] can be detected in the Pt layer *via* ISHE by sweeping the applied magnetic field along the y axis. Figure 4f shows the $V_{SSE}(H)$ as a function of the applied magnetic field at various temperatures. The sign of $V_{SSE}(H)$ changes as the magnetic field polarity reverses, which agrees with the M-H hysteresis loops in Figure 1f. This confirms that the measured $V_{SSE}(H)$ originates from the spin current induced by ∇T for GdIG/Pt. Interestingly, the sign of the amplitude of $V_{SSE}(H)$ at the positive field at 300 K is opposite to that at 125 K, but identical to that at 10 K.

The amplitudes of the SP- and SSE-driven ISHE voltages as a function of temperature are shown in Figure 5a. It was established that the sign of $V_{SSE} = (V_{SSE}(+H) - V_{SSE}(-H))/2$ reverses

at ~72 K and reverses again at the magnetic compensation temperature (~200 K)[54]. In contrast, the sign inversion was not observed in the SP experiment of the GdIG/Pt systems; the sign of V_{SP} remains negative over the measured temperature range. It appears counterintuitive that the sign of V_{SP} does not change at T_M, at which point the moments of the Fe and Gd sublattices reverse [see the schematic illustration in Figure 1g]. Moreover, the amplitude of V_{SP} decreases with temperature approaching to T_M. These results raise the question why the direction of the coherent and incoherent spin currents varies differently upon changing temperature, particularly when the temperature crosses the T_M.

To unravel the origin of the discrepancy in the sign variation in the SSE and SP experiments, we calculated the spin-wave spectra of GdIG at different temperatures, as shown in Figure 5b-d, in which the orange and navy lines represent the α modes (left-handed) and β modes (right-handed), respectively. The α and β modes host opposite spin polarizations. Noticeably, the spin-wave spectrum ($T < T_M$) of GdIG above the β_1 branch, dominated by the Fe sublattices, is very similar to those of YIG[55], and the additional α_1 modes below the β_1 branch mainly originate from the contribution of the Gd sublattices. In the SSE experiments, the temperature-dependent V_{SSE} predominantly depends on the thermal occupation of the α and β modes. At very low temperatures, the thermal magnons from the β modes are frozen out owing to the large magnon gap. Consequently, below ~72 K, the contributions of the α modes dominate the SSE signals, while those of the β modes are almost negligible. Increasing temperature above 72 K, the magnon gap is gradually suppressed; therefore, the thermal magnons of the β modes are continuously activated[25]. Due to the stronger exchange coupling between the Fe 3*d*-electrons and the Pt conduction electrons, compared to that for the local Gd 4*f*-electrons, the contribution from the β modes become dominant in the SSE signals, causing the change of the V_{SSE} sign at ~72 K[54]. In contrast, the competition between the α and β modes is absent in the SP experiments because only the lowest α_1 mode in the GHz frequency range is uniformly excited under the FMR condition. Consequently, the sign of V_{SP} remains unchanged across ~72 K.

As the moment of Gd rapidly decreases with further increasing temperature, the net magnetization nearly vanishes with temperature up to ~T_M. Meanwhile, V_{SP} decreases owing to the small net magnetization and the large damping. With increasing the temperature further

above T_M, the net magnetization is dominated by the Fe sublattices, and aligned by the external magnetic field, resulting in the polarization inversion of the spin-wave spectra across T_M[56]. Thus, the sign change of V_{SSE} reverses at ~200 K. It appears that V_{SP} should reverse as a consequence of the α modes being converted into the β modes above T_M. Nevertheless, the red shift of the β modes occurs with increasing temperature [see Figure 5b-d]. Above T_M, the frequency of the lowest β modes is lower than that of the α modes [see Figure 5d]. Upon applying an external magnetic field, the polarizations of all the magnon bands flip. As a result, the lowest β mode behaves similarly to the lowest α mode below T_M under the FMR condition. Therefore, the sign of V_{SP} remains unchanged across T_M.

Conclusion

In conclusion, we systematically investigated the SP and magnetic damping in insulating compensated ferrimagnetic GdIG films. In addition to the divergent bulk damping in GdIG films close to the compensation temperature, we observed the divergence of the nonlocal damping induced by SP in GdIG-based heterostructures. Furthermore, different from the case of the incoherent spin currents generated by SSE, the direction of the coherent spin currents generated by SP does not change when varying the sample temperatures. The physical reason behind these observations was explained by the ferrimagnetic SP model and the evolution of the handedness-related spin-wave spectra as the temperature increased across T_M. The spin-mixing conductance is self-consistently determined in the theoretical framework of ferrimagnetic SP. Our work offers significant fundamental insight into the SP and magnetic damping in compensated ferrimagnets, which will facilitate their applications in magnonics.

Experimental Section

$Gd_3Fe_5O_{12}$ (GdIG, thickness: 35 nm) films were grown on (111)-oriented $Gd_{2.6}Ca_{0.4}Ga_{4.1}Mg_{0.25}Zr_{0.65}O_{12}$ (sGGG) substrates by PLD at a laser repetition frequency of 5 Hz. During deposition, the substrate temperature was set to 640 K, and the oxygen pressure was 85 mTorr. After deposition, the samples were cooled to room temperature at a rate of 5 K/min. Thereafter, they were transferred to a magnetron sputter system, where a 10 nm-thick Pt layer was deposited at room temperature. Magnetization measurements were performed using a

magnetic property measurement system (MPMS3, Quantum Design). The structures were characterized using STEM (Titan 80-300, FEI) after the sample was prepared using a focused ion beam (Helios 450, FEI).

The FMR and SP-induced ISHE measurements were performed using a coplanar waveguide-based setup in a physical property measurement system (PPMS, Quantum Design). Microwave excitation was generated using a microwave signal generator (R&S®SMB100A). By sweeping the magnetic field, the FMR transmission signals modulated by a Helmholtz coil were read by the Stanford Research SR830 lock-in amplifiers based on a phase-sensitive technique. The SP-driven ISHE signals were read using a Keithley 2182 meter. The details of the FMR and SP-induced ISHE measurements are provided in the SI.

The devices for the SSE measurements were fabricated using a standard photolithography technique and Ar ion milling. The GdIG/Pt film was first patterned into Hall bars with a width of 50 μm, after which an 80 nm-thick SiO_2 film was deposited on it as an insulating layer. The temperature gradient was applied using a heater strip [Ti(5 nm)/Pt(40 nm)] deposited on the SiO_2 layer. Ti(10 nm)/Au(190 nm) stacks were deposited as electrical contacts. The SSE measurements were performed in a PPMS chamber. A temperature gradient along the z axis was built by a heater striper with a charge current of 10 mA (Keithley 6221 meter). The temperature gradient induced SSE-generated and driven inverse spin Hall voltages in the sweeping magnetic field along the y axis, which were detected using the Keithley 2182 meter.

Supporting Information

Supporting Information is available from the Wiley Online Library or from the author.

Acknowledgments

The study reported was funded by King Abdullah University of Science and Technology, Office of Sponsored Research (OSR) under Award Nos. OSR 2018-3717-CRG7 and OSR-2019-CRG8-4081. The study was also supported by the National Natural Science Foundation of China (No. 11974047) and the Fundamental Research Funds for the Central Universities.

Conflict of Interest

The authors declare no competing interests.

References

[1] Y. Kajiwara, K. Harii, S. Takahashi, J. Ohe, K. Uchida, M. Mizuguchi, H. Umezawa, H. Kawai, K. Ando, K. Takanashi, S. Maekawa, E. Saitoh, *Nature* **2010**, 464, 262.

[2] A. V. Chumak, V. I. Vasyuchka, A. A. Serga, B. Hillebrands, *Nat. Phys.* **2015**, 11, 453.

[3] A. Barman, G. Gubbiotti, S. Ladak, A. O. Adeyeye, M. Krawczyk, J. Grafe, C. Adelmann, S. Cotofana, A. Naeemi, V. I. Vasyuchka, B. Hillebrands, S. A. Nikitov, H. Yu, D. Grundler, A. V. Sadovnikov, A. A. Grachev, S. E. Sheshukova, J. Y. Duquesne, M. Marangolo, G. Csaba, W. Porod, V. E. Demidov, S. Urazhdin, S. O. Demokritov, E. Albisetti, D. Petti, R. Bertacco, H. Schultheiss, V. V. Kruglyak, V. D. Poimanov, S. Sahoo, J. Sinha, H. Yang, M. Munzenberg, T. Moriyama, S. Mizukami, P. Landeros, R. A. Gallardo, G. Carlotti, J. V. Kim, R. L. Stamps, R. E. Camley, B. Rana, Y. Otani, W. Yu, T. Yu, G. E. W. Bauer, C. Back, G. S. Uhrig, O. V. Dobrovolskiy, B. Budinska, H. Qin, S. van Dijken, A. V. Chumak, A. Khitun, D. E. Nikonov, I. A. Young, B. W. Zingsem, M. Winklhofer, *J. Phys. Condens. Matter.* **2021**, 33, 413001.

[4] R. Urban, G. Woltersdorf, B. Heinrich, *Phys. Rev. Lett.* **2001**, 87, 217204.

[5] S. Mizukami, Y. Ando, T. J. J. o. m. Miyazaki, m. materials, *J. Magn. Magn. Mater* **2001**, 226, 1640.

[6] Y. Tserkovnyak, A. Brataas, G. E. Bauer, *Phys. Rev. Lett.* **2002**, 88, 117601.

[7] Y. Tserkovnyak, A. Brataas, G. E. W. Bauer, *Phys. Rev. B* **2002**, 66, 224403.

[8] R. Cheng, J. Xiao, Q. Niu, A. Brataas, *Phys. Rev. Lett.* **2014**, 113, 057601.

[9] T. Jungwirth, X. Marti, P. Wadley, J. Wunderlich, *Nat. Nanotech.* **2016**, 11, 231.

[10] V. Baltz, A. Manchon, M. Tsoi, T. Moriyama, T. Ono, Y. Tserkovnyak, *Rev. Mod. Phys.* **2018**, 90, 015005.

[11] J. Li, C. B. Wilson, R. Cheng, M. Lohmann, M. Kavand, W. Yuan, M. Aldosary, N. Agladze, P. Wei, M. S. Sherwin, J. Shi, *Nature* **2020**, 578, 70.

[12] P. Vaidya, S. A. Morley, J. van Tol, Y. Liu, R. Cheng, A. Brataas, D. Lederman, E. Del Barco, *Science* **2020**, 368, 160.

[13] I. Boventer, H. T. Simensen, A. Anane, M. Klaui, A. Brataas, R. Lebrun, *Phys. Rev. Lett.* **2021**, 126, 187201.

[14] H. Wang, Y. Xiao, M. Guo, E. Lee-Wong, G. Q. Yan, R. Cheng, C. R. Du, *Phys. Rev. Lett.* **2021**, 127, 117202.

[15] A. Kamra, W. Belzig, *Phys. Rev. Lett.* **2017**, 119, 197201.

[16] K. J. Kim, S. K. Kim, Y. Hirata, S. H. Oh, T. Tono, D. H. Kim, T. Okuno, W. S. Ham, S. Kim, G. Go, Y. Tserkovnyak, A. Tsukamoto, T. Moriyama, K. J. Lee, T. Ono, *Nat. Mater.* **2017**, 16, 1187.

[17] J. Shim, S. J. Kim, S. K. Kim, K. J. Lee, *Phys. Rev. Lett.* **2020**, 125, 027205.

[18] C. Kim, S. Lee, H. G. Kim, J. H. Park, K. W. Moon, J. Y. Park, J. M. Yuk, K. J. Lee, B. G. Park, S. K. Kim, K. J. Kim, C. Hwang, *Nat. Mater.* **2020**, 19, 980.

[19] J. Finley, L. Liu, *Appl. Phys. Lett.* **2020**, 116, 110501.

[20] S. K. Kim, G. S. D. Beach, K. J. Lee, T. Ono, T. Rasing, H. Yang, *Nat. Mater.* **2022**, 21, 24.

[21] L. Sheng, J. Chen, H. Wang, H. Yu, *J. Phys. Soc. Japan* **2021**, 90, 081005.

[22] R. Pauthenet, *J. Appl. Phys.* **1958**, 29, 253.

[23] A. B. Harris, *Phys. Rev.* **1963**, 132, 2398.

[24] L. Liensberger, A. Kamra, H. Maier-Flaig, S. Geprags, A. Erb, S. T. B. Goennenwein, R. Gross, W. Belzig, H. Huebl, M. Weiler, *Phys. Rev. Lett.* **2019**, 123, 117204.

[25] K. Shen, *Phys. Rev. B* **2019**, 99, 024417.

[26] Y. Fan, J. Finley, J. Han, M. E. Holtz, P. Quarterman, P. Zhang, T. S. Safi, J. T. Hou, A. J. Grutter, L. Liu, *Adv. Mater.* **2021**, e2008555.

[27] R. Sun, S. Yang, X. Yang, A. Kumar, E. Vetter, W. Xue, Y. Li, N. Li, Y. Li, S. Zhang, B. Ge, X. Q. Zhang, W. He, A. F. Kemper, D. Sun, Z. H. Cheng, *Adv. Mater.* **2020**, e2005315.

[28] S. Geschwind, L. R. Walker, *J. Appl. Phys.* **1959**, 30, S163.

[29] C. Kittel, *Phys. Rev.* **1948**, 73, 155.

[30] Y. Sun, H. Chang, M. Kabatek, Y. Y. Song, Z. Wang, M. Jantz, W. Schneider, M. Wu, E. Montoya, B. Kardasz, B. Heinrich, S. G. te Velthuis, H. Schultheiss, A. Hoffmann, *Phys. Rev. Lett.* **2013**, 111, 106601.
[31] M. A. W. Schoen, D. Thonig, M. L. Schneider, T. J. Silva, H. T. Nembach, O. Eriksson, O. Karis, J. M. Shaw, *Nat. Phys.* **2016**, 12, 839.
[32] M. Guan, L. Wang, S. Zhao, Z. Zhou, G. Dong, W. Su, T. Min, J. Ma, Z. Hu, W. Ren, Z. G. Ye, C. W. Nan, M. Liu, *Adv. Mater.* **2018**, e1802902.
[33] Y. Tserkovnyak, A. Brataas, G. E. Bauer, B. I. Halperin, *Rev. Mod. Phys.* **2005**, 77, 1375.
[34] S. S. Kalarickal, P. Krivosik, M. Wu, C. E. Patton, M. L. Schneider, P. Kabos, T. J. Silva, J. P. Nibarger, *J. Appl. Phys.* **2006**, 99, 093909.
[35] X. Tao, Q. Liu, B. Miao, R. Yu, Z. Feng, L. Sun, B. You, J. Du, K. Chen, S. Zhang, L. Zhang, Z. Yuan, D. Wu, H. Ding, *Sci. Adv.* **2018**, 4, eaat1670.
[36] H. Maier-Flaig, S. Klingler, C. Dubs, O. Surzhenko, R. Gross, M. Weiler, H. Huebl, S. T. B. Goennenwein, *Phys. Rev. B* **2017**, 95, 214423.
[37] B. Calhoun, J. Overmeyer, W. J. P. R. Smith, *Phys. Rev.* **1957**, 107, 993.
[38] Y. M. Lu, Y. Choi, C. M. Ortega, X. M. Cheng, J. W. Cai, S. Y. Huang, L. Sun, C. L. Chien, *Phys. Rev. Lett.* **2013**, 110, 147207.
[39] T. Kikkawa, M. Suzuki, J. Okabayashi, K.-i. Uchida, D. Kikuchi, Z. Qiu, E. Saitoh, *Phys. Rev. B* **2017**, 95.
[40] K. Roy, *Phys. Rev. B* **2017**, 96, 174432.
[41] T. Kimura, J. Hamrle, Y. Otani, *Phys. Rev. B* **2005**, 72, 014461.
[42] M. Caminale, A. Ghosh, S. Auffret, U. Ebels, K. Ollefs, F. Wilhelm, A. Rogalev, W. E. Bailey, *Phys. Rev. B* **2016**, 94, 014414.
[43] E. Montoya, B. Heinrich, E. Girt, *Phys. Rev. Lett.* **2014**, 113, 136601.
[44] A. M. Goncalves, F. Garcia, H. K. Lee, A. Smith, P. R. Soledade, C. A. C. Passos, M. Costa, N. M. Souza-Neto, I. N. Krivorotov, L. C. Sampaio, I. Barsukov, *Sci. Rep.* **2018**, 8, 2318.
[45] P. Omelchenko, E. A. Montoya, E. Girt, B. Heinrich, *Phys. Rev. Lett.* **2021**, 127, 13720.
[46] G. Wu, D. Wu, Y. Ren, Q. Y. Jin, Z. Zhang, *Phys. Rev. B* **2021**, 103, 014419.
[47] A. Kamra, R. E. Troncoso, W. Belzig, A. Brataas, *Phys. Rev. B* **2018**, 98, 184402.
[48] B. Heinrich, C. Burrowes, E. Montoya, B. Kardasz, E. Girt, Y. Y. Song, Y. Sun, M. Wu, *Phys. Rev. Lett.* **2011**, 107, 066604.
[49] A. Hamadeh, O. d'Allivy Kelly, C. Hahn, H. Meley, R. Bernard, A. H. Molpeceres, V. V. Naletov, M. Viret, A. Anane, V. Cros, S. O. Demokritov, J. L. Prieto, M. Munoz, G. de Loubens, O. Klein, *Phys. Rev. Lett.* **2014**, 113, 197203.
[50] L. Soumah, N. Beaulieu, L. Qassym, C. Carrétéro, E. Jacquet, R. Lebourgeois, J. Ben Youssef, P. Bortolotti, V. Cros, A. Anane, *Nat. Commun.* **2018**, 9, 3355.
[51] E. Saitoh, M. Ueda, H. Miyajima, G. Tatara, *Appl. Phys. Lett.* **2006**, 88, 182509.
[52] K.-i. Uchida, H. Adachi, T. Ota, H. Nakayama, S. Maekawa, E. Saitoh, *Appl. Phys. Lett.* **2010**, 97, 172505.
[53] H. Liu, H. Malissa, R. M. Stolley, J. Singh, M. Groesbeck, H. Popli, M. Kavand, S. K. Chong, V. V. Deshpande, J. S. Miller, C. Boehme, Z. V. Vardeny, *Adv. Mater.* **2020**, 32, e2002663.
[54] S. Geprägs, A. Kehlberger, F. Della Coletta, Z. Qiu, E. J. Guo, T. Schulz, C. Mix, S. Meyer, A. Kamra, M. Althammer, H. Huebl, G. Jakob, Y. Ohnuma, H. Adachi, J. Barker, S. Maekawa, G. E. Bauer, E. Saitoh, R. Gross, S. T. Goennenwein, M. Klaui, *Nat. Commun.* **2016**, 7, 10452.
[55] K. Shen, *New J. Phys.* **2018**, 20, 043025.
[56] Y. Ohnuma, H. Adachi, E. Saitoh, S. Maekawa, *Phys. Rev. B* **2013**, 87, 014423.

Figure

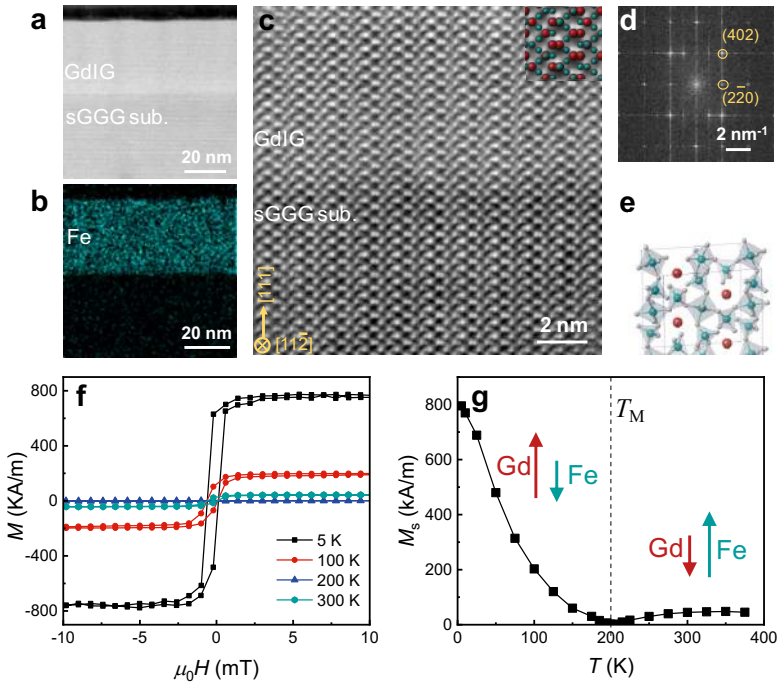

Figure 1. Structure and magnetic properties of the GdIG film. a) STEM cross-sectional image. b) EDX color mapping of Fe. c) Atomic-resolution STEM image. The enlarged part shows the atomic model overlayed on the real atoms. The green and red balls represent the Fe and Gd atoms. d) Corresponding FFT patterns of GdIG. e) Schematic of the crystal structure of GdIG. The green, red, and gray balls represent the Fe, Gd, and O atoms, respectively. f) Magnetic hysteresis loop of the GdIG film. g) Saturation magnetization (M_s) as a function of temperature. The arrows show the magnetic states above and below the magnetic compensation temperature, respectively.

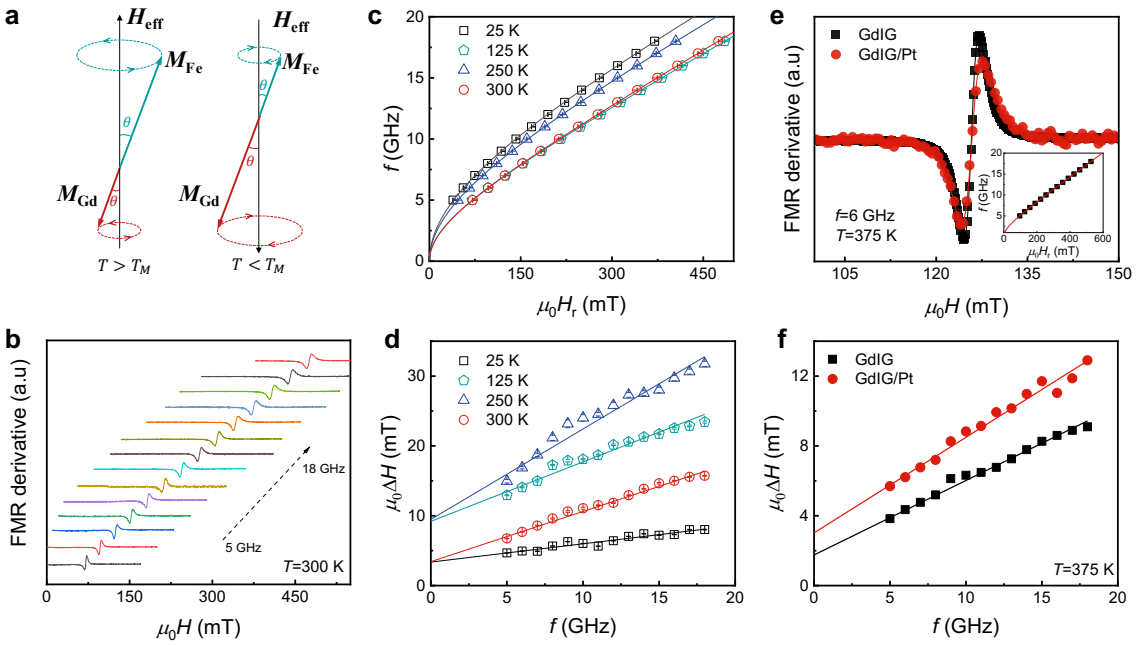

Figure 2. FMR measurements of the GdIG and GdIG/Pt films. a) Low-frequency uniform modes in the FMR measurements. b) FMR spectra of GdIG (thickness: 35 nm) at 300 K. c) Frequency dependence of the resonant magnetic field (H_r) at various temperatures in GdIG. d) Resonant linewidth as a function of frequency at various temperatures in GdIG. e) Comparison of the FMR spectra for GdIG (35 nm)/Pt (10 nm) and GdIG (35 nm) at f = 6 GHz at 375 K. The inset shows H_r versus f for GdIG/Pt. f) Comparison of the linewidth versus frequency for GdIG/Pt and GdIG at 375 K.

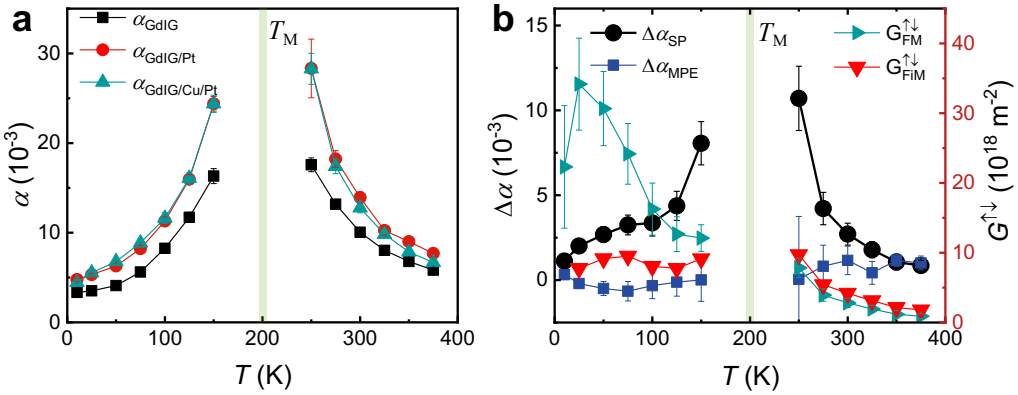

Figure 3. Magnetic damping at various temperatures. a) Values of the effective Gilbert damping as a function of the temperature for the GdIG, GdIG/Pt and GdIG/Cu/Pt samples. b) Damping contributions from the SP effect and the MPE, and the evaluated spin-mixing conductance based on ferromagnetic and ferrimagnetic SP models. The color region corresponds to the magnetic compensation temperature T_M.

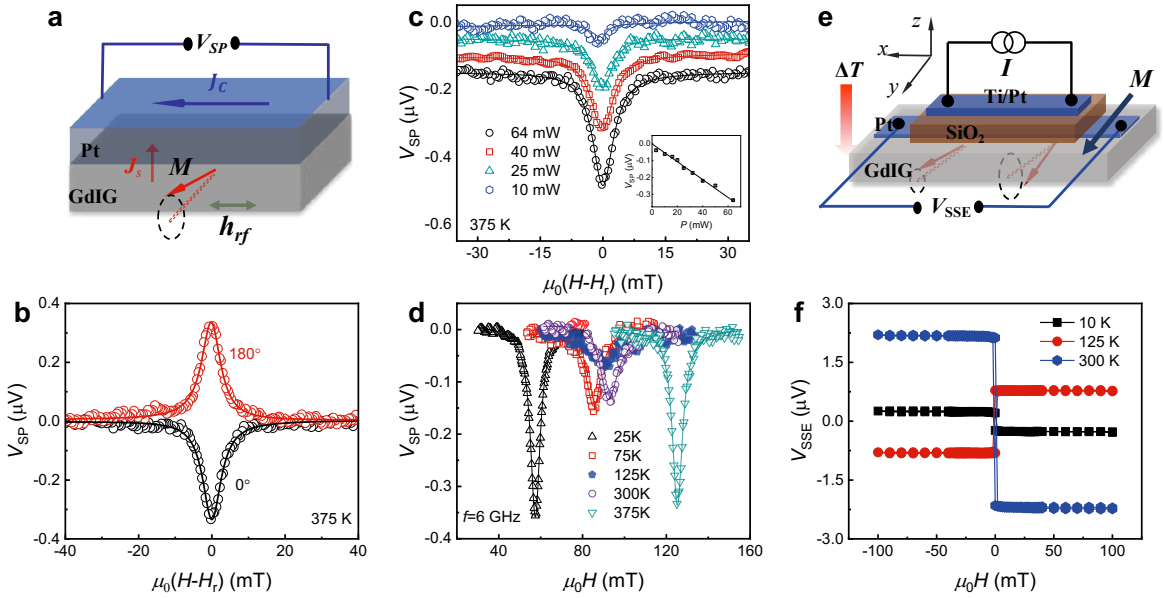

Figure 4. Observation of the SP- and SSE-driven ISHE in GdIG/Pt. a) Schematic of the SP measurements. b) ISHE voltage (V_{SP}) nearby FMR condition ($H = H_r$) at P = 64 mW with sweeping positive (black) and negative (red) magnetic fields at 375 K. c) Microwave power dependence of V_{SP} at 375 K. The inset shows the extracted V_{SP} under the FMR condition. d) ISHE spectra at P = 64 mW in the SP experiments at various temperatures. e) Schematic of the SSE measurements. f) SSE signal (V_{SSE}) as a function of the applied magnetic field at various temperatures.

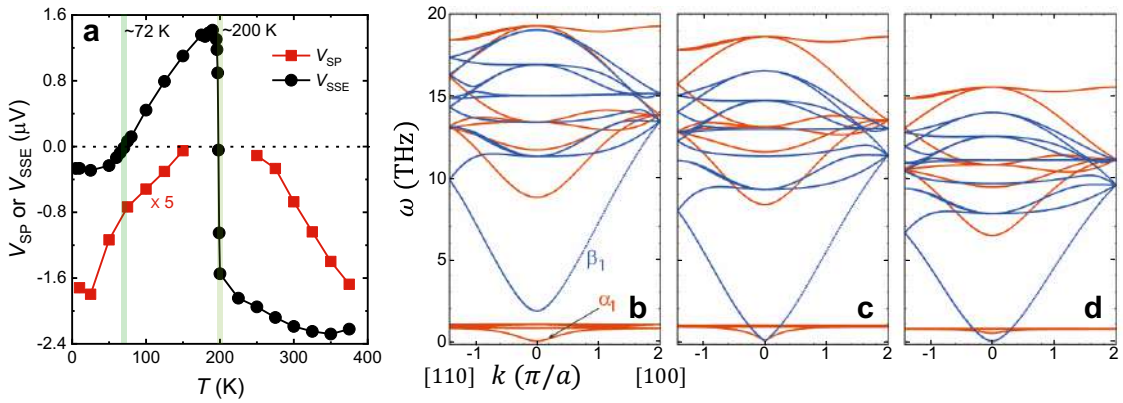

Figure 5. SP- and SSE-driven ISHE voltages and spin-wave spectra at various temperatures. a) Comparison of the SP- and SSE-driven ISHE voltages as functions of temperature for the GdIG/Pt samples. The sign of V_{SSE} reverses at the corresponding temperatures (color regions). V_{SP} is multiplied by a factor of 5 for comparison. The calculated spin-wave spectra at b) $T < T_M$, c) $T \sim T_M$ and d) $T > T_M$. The orientations of the Gd moment are set to the same direction in all calculated spectra.

Table of Contents

Yan Li, Dongxing Zheng, Bin Fang, Chen Liu, Chenhui Zhang, Aitian Chen, Yinchang Ma, Ka Shen, Haoliang Liu, Aurélien Manchon, and Xixiang Zhang**

Unconventional spin pumping and magnetic damping in an insulating compensated ferrimagnet

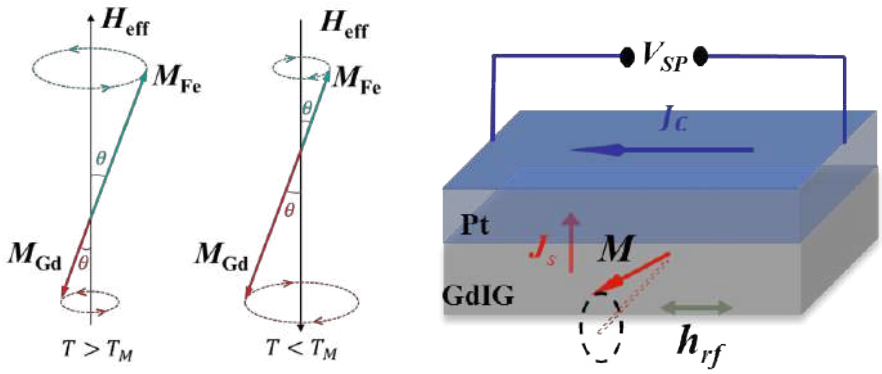

An unconventional spin pumping together with the divergent nonlocal magnetic damping is unambiguously reported in the compensated ferrimagnetic $Gd_3Fe_5O_{12}$-based heterostructures. The coherent and incoherent spin currents undergo a distinct direction change with the variation of temperature. The underlying physical mechanisms are self-consistently clarified by the ferrimagnetic counterpart of spin pumping and the handedness-related spin-wave spectra.